Hyperfine Interactions 125 (2000) 149–172

CONUSS and PHOENIX: Evaluation of nuclear resonant scattering data

W. Sturhahn

Advanced Photon Source, Argonne National Laboratory, Argonne, IL 60439, USA

Evaluation methods for data obtained by nuclear resonant scattering techniques are discussed. The CONUSS software package for the interpretation of time or energy spectra from coherent elastic nuclear resonant scattering, i.e., forward scattering and Bragg/Laue scattering, is presented. The analysis of phonon spectra obtained by incoherent nuclear resonant scattering is demonstrated using the PHOENIX software.

1. Introduction

The combination of nuclear resonant scattering (NRS) and synchrotron radiation prompted novel techniques for the study of condensed matter. The most remarkable developments may be synchrotron Mössbauer spectroscopy and phonon spectroscopy employing incoherent NRS. Ample examples supporting this assessment can be found in the present book [1]. In this contribution, software packages are described that offer substantial help in the analysis of typical spectra of either method. The first part of the paper explains how the CONUSS (COherent NUclear resonant Scattering by Single crystals) programs permit derivation of hyperfine parameters from time spectra of nuclear forward scattering (NFS), nuclear Bragg scattering, or nuclear Laue scattering. The emphasis will be on NFS, because of its broader range of applications. The CONUSS program package grew simultaneously with experimental studies of coherent elastic NRS. Such experiments were initially performed on single crystals, e.g., Gerdau et al. [2,3] using YIG, Faigel et al. [4] using Fe_2O_3, and van Bürck et al. [5] using $FeBO_3$, to name a few. CONUSS also served to evaluate data of the first experiment to use NFS; van Bürck et al. [6] combined a nuclear Bragg reflection of $FeBO_3$ with Invar absorbers. The spectroscopic capabilities of coherent elastic NRS were greatly enhanced after technical difficulties related to NFS were overcome by the high-energy resolution monochromators of Hastings et al. [7] and the avalanche photodiode detectors of Kishimoto [8]. The high brightness of third-generation synchrotron radiation sources promoted NFS to a viable spectroscopy. Using high-brightness synchrotron radiation sources, Toellner et al. [9] and Siddons et al. [10] could show that polarization filtering can be advantageously combined with NFS. In this case, Alp et al. [11] point out that one observes the optical activity of the sample around the nuclear resonance and benefits from the considerable suppression of the nonresonant counting rate. The

CONUSS programs and other evaluation software [12] now play important roles in the parameterization of experimental data. A brief description of CONUSS given by Sturhahn [13] was followed up by Sturhahn and Gerdau in a paper about the theoretical basis of the software [14].

In the second part of this paper, the PHOENIX (PHOnon Excitation by Nuclear Inelastic scattering of X-rays) software is introduced. The use of this program facilitates the derivation of the phonon density of states from the typical incoherent NRS spectrum along with several parameters pertinent to the local dynamics of the lattice. The application of incoherent NRS as a tool for investigations of lattice vibrations was only recently introduced by Seto et al. [15], Sturhahn et al. [16], and Chumakov et al. [17]. The present status of the method is explained elsewhere in this book. Both software packages, CONUSS and PHOENIX, are freely available from the author.

2. The CONUSS software

The data from experiments involving coherent elastic NRS usually consist of time spectra. The time spectrum is a collection of events, each of which registers the time span between arrival of the synchrotron radiation pulses and arrival of a scattered photon. Here the sample contains nuclei with a Mössbauer resonance, and hence the decay time of scattering contributions from the nuclei is dictated by the nuclear lifetime. In addition, oscillations are observed that originate in nuclear level splitting. Also quite common is the thickness-dependent acceleration of nuclear decay or “speed-up”. The combination of both effects may render complicated shapes for the time spectra. In this scenario, the purpose of the CONUSS programs can be defined as follows:

– Calculation of time and energy spectra for given properties of sample and incident radiation.
– Comparison of calculated spectra with measured data including the automatic adjustment of parameters with the objective to obtain the best agreement of theory and data.

The above topics will be addressed individually. In the appendix, calculations of integrated delayed counting rates for various NFS scenarios are presented. These data provide valuable information for the design of NFS experiments.

2.1. Calculation of time and energy spectra

A microscopic model for NRS is needed to prepare suitable procedures. Hannon and Trammell [18] treated NRS as a quantum-electrodynamical scattering process of a weak photon field incorporating the particular properties of nuclear resonances. This picture has the advantage of being microscopic, i.e., one can build a program “from the inside out”. In CONUSS, the basic nuclear properties and the basic properties of the crystal structure are defined by the parameters listed in table 1. Next, the

Table 1
List of parameters describing basic nuclear properties and basic crystal properties.

Symbol	Parameter
M	Mass of the resonant isotope.
I, I'	Spin numbers of nuclear ground and excited states.
g, g'	g-factors of nuclear ground and excited states.
Q, Q'	Quadrupole moments of nuclear ground and excited states.
$t_{1/2}$	Half life time of the nuclear excited state.
α'	Internal conversion factor.
E_0	Nuclear transition energy.
L, λ	Multipolarity and parity of the nuclear transition.
β	Interference coefficient of the nuclear transition.
Z	Charge of the nucleus.
A	Isotopic abundance.
a, b, c	Lengths of base vectors of the unit cell.
$\angle(b,c), \angle(a,c), \angle(a,b),$	Angles between base vectors of the unit cell.
$T_{\rm D}$	Debye temperature of the material.
T	Actual temperature of the material.

interaction between the nucleus and its environment is considered. CONUSS offers a choice between static hyperfine interactions and randomly fluctuating hyperfine fields as described by Blume and Tjon [19]. A set of hyperfine parameters together with the coordinates of the Mössbauer atoms in the unit cell constitute a site. The maximum number of sites that may be defined is not limited in principle, i.e., the value will depend on computing resources only. It is possible to combine sites with fluctuating and static hyperfine interactions as needed. A site with static hyperfine fields is characterized by a list of parameters that is provided in table 2. The notions of isomer shift, magnetic hyperfine field, quadrupole splitting, and asymmetry parameter of the electric field gradient (EFG) tensor are commonly known. The Euler angles rotate the main axes system of the EFG tensor, which can be obtained by diagonalization, into a basis that is determined by the crystal lattice. The direction of the magnetic hyperfine field is defined with respect to the direction of the external magnetic field and an additional orthogonal reference vector using the angular coordinates θ and φ. The related geometry is displayed in figure 1. One also encounters situations where the magnitude of the hyperfine field depends on its direction. Such cases are included by defining asymmetry parameters of the magnetic hyperfine field as follows. Assume the magnitude of the magnetic hyperfine field is written as

$$B = \sqrt{B_x^2 \cos^2 \gamma_x + B_y^2 \cos^2 \gamma_y + B_z^2 \cos^2 \gamma_z}, \tag{1}$$

where $B_{x,y,z}$ are the main values with regard to the local symmetry axes, which are identical to the main axes of the EFG. $\gamma_{x,y,z}$ are the angles of the magnetic hyperfine field with respect to the local symmetry axes. $B_{x,y,z}$ may be replaced by the isotropic field value B_0, polar asymmetry $\xi_{\rm p}$, and azimuthal asymmetry $\xi_{\rm a}$. The relationships

Table 2
Hyperfine interaction parameters that define a particular site.

Symbol	Parameter
δE_0	Isomer shift.
$eQ'V_{zz}/2$	Quadrupole splitting of excited nuclear state.
η	Asymmetry parameter of EFG tensor.
α, β, γ	Euler angles of EFG main axes.
B_0	Magnetic hyperfine field, isotropic part.
$\xi_{\rm p}$	Polar asymmetry of magnetic hyperfine field according to eq. (2).
$\xi_{\rm a}$	Azimuthal asymmetry of magnetic hyperfine field according to eq. (2).
θ, φ	Polar and azimuthal angles of magnetic hyperfine field (see figure 1).
$\{x_j, y_j, z_j\}$	Positions of Mössbauer atoms in the unit cell.

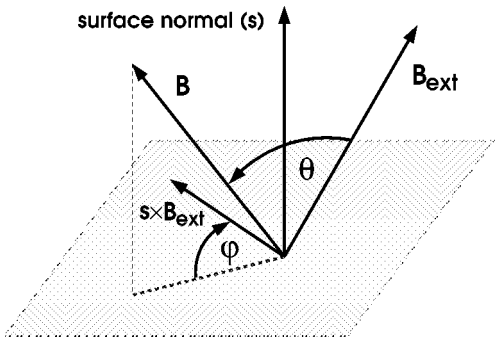

Figure 1. Direction of the magnetic hyperfine field **B**. The angles θ and φ are used as input parameters in CONUSS. The reference system is constructed from the direction of the external magnetic field $\mathbf{B}_{\rm ext}$ and the cross product of surface normal and $\mathbf{B}_{\rm ext}$ as displayed above. If the external field points along the surface normal the projection of a unit cell base vector onto the surface replaces the cross product as reference vector for the angle φ.

are

$$
\begin{aligned}
B_0 &= \sqrt{\frac{1}{3}\big(B_x^2 + B_y^2 + B_z^2\big)}, \\
\xi_{\rm p} &= \frac{1}{6B_0^2}\big(2B_z^2 - B_y^2 - B_x^2\big), \\
\xi_{\rm a} &= \frac{B_y^2 - B_x^2}{B_y^2 + B_x^2}.
\end{aligned}
\tag{2}
$$

The values of the asymmetries are restricted to the ranges $\xi_{\rm p} \in [-0.5, 1]$ and $\xi_{\rm a} \in [-1, 1]$. The angular dependence of the magnetic hyperfine field is now given by

$$
B(\theta_{\rm B}, \phi_{\rm B}) = B_0\sqrt{1 + \xi_{\rm p}\big(3\cos^2\theta_{\rm B} - 1\big) + \xi_{\rm a}(\xi_{\rm p} - 1)\sin^2\theta_{\rm B}\cos 2\phi_{\rm B}}, \tag{3}
$$

where $B_0, \theta_{\rm B}, \phi_{\rm B}$ are the polar coordinates with respect to the main axes of the EFG. The angles are calculated internally from the direction of the hyperfine field and the

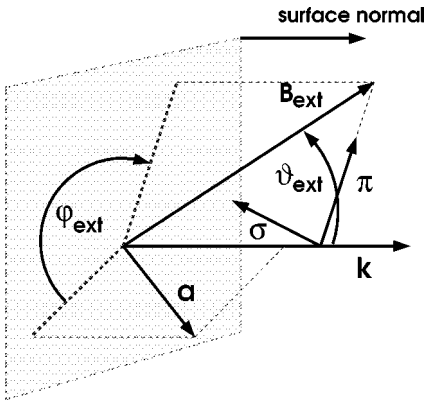

Figure 2. Forward scattering geometry. The incident radiation with wave vector **k** is parallel to the surface normal. The angles $\vartheta_{\rm ext}$ and $\varphi_{\rm ext}$ provide the direction of the external magnetic field $\mathbf{B}_{\rm ext}$. The projection of a unit cell base vector **a** onto the surface and **k** serve as reference vectors. The polarization vector σ is defined perpendicular to **k** and $\mathbf{B}_{\rm ext}$. If the external field points along the wave vector **k** the polarization vector σ is defined perpendicular to **k** and unit cell base vector **a**.

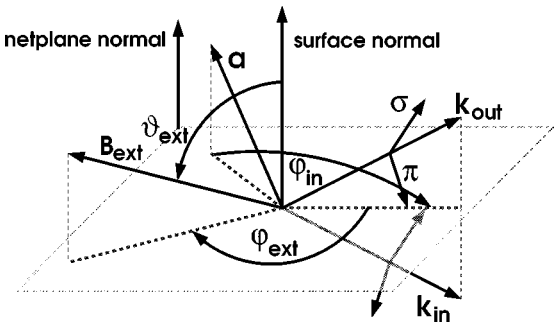

Figure 3. Geometry for symmetric Bragg scattering. The normal of the reflecting netplanes is parallel to the surface normal. The direction of the incident wave vector $\mathbf{k}_{\rm in}$ is determined by the angle $\varphi_{\rm in}$ and the Bragg condition. **a** is a unit cell base vector. The angles $\vartheta_{\rm ext}$ and $\varphi_{\rm ext}$ provide the direction of the external magnetic field $\mathbf{B}_{\rm ext}$. The projection of $\mathbf{k}_{\rm in}$ onto the surface and the surface normal serve as reference vectors. The polarization vector σ is perpendicular to the scattering plane that is defined by $\mathbf{k}_{\rm in}$ and the reflected wave vector $\mathbf{k}_{\rm out}$.

orientation of the EFG main axes that are specified by the Euler angles. The common magnetic dipole field results from an approximation of the previous equation for $|\xi_{\rm p}| \ll 1$, $\xi_{\rm a} = 0$, i.e., $B_{\rm dip} = \xi_{\rm p} B_0$. An isotropic magnetic hyperfine field results from $\xi_{\rm p} = \xi_{\rm a} = 0$. The external field is given relative to the crystal basis and wave vectors of incident and scattered radiation depending of the scattering scenario. In figure 2, the situation is displayed for cases of forward scattering. Figures 3 and 4 explain the relationships for symmetric and asymmetric Bragg scattering. Direction and magnitude of the external magnetic field are defined by parameters given in table 3. The nuclear level splitting and the corresponding eigenvectors are obtained by numerically solving

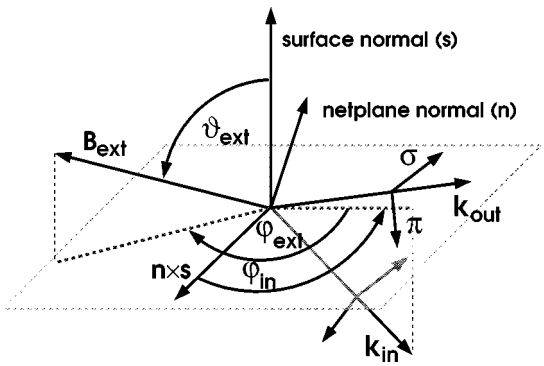

Figure 4. Geometry for asymmetric Bragg scattering. The normals of the reflecting netplanes and the surface are not parallel to each other. The direction of the incident wave vector $\mathbf{k}_{\text{in}}$ is determined by the angle φ_{in} as shown and the Bragg condition. The angles ϑ_{ext} and φ_{ext} provide the direction of the external magnetic field $\mathbf{B}_{\text{ext}}$. The projection of $\mathbf{k}_{\text{in}}$ onto the surface and the cross product of netplane normal and surface normal serve as reference vectors. The polarization vector σ is perpendicular to the scattering plane that is defined by $\mathbf{k}_{\text{in}}$ and the reflected wave vector $\mathbf{k}_{\text{out}}$.

Table 3
Miscellaneous parameters used by the CONUSS software.

Symbol	Parameter
s_1, s_2, s_3	Components of the surface normal.
B_{ext}	Magnitude of external magnetic field.
φ_{ext}	Angle between the incident wave vector and external magnetic field, in each case projected onto the surface (see also figures 2–4).
ϑ_{ext}	Angle between external magnetic field and surface normal (see figures 2–4).
h, k, l	Miller indices of the reflection.
φ_{in}	Angle between the incident wave vector projected onto the surface and a reference vector (see figures 2–4).
D	Thickness of the crystal.
$[E_1, E_2]$	Energy interval around the unsplit and unshifted nuclear resonance used in the calculation.
$[\theta_1, \theta_2]$	Angle interval around the direction of the incident wave vector that satisfies the Bragg condition.
Z_j	Nuclear charges of the nonresonant atoms.
$\{x_j, y_j, z_j\}$	Positions of nonresonant atoms in the unit cell.

the diagonalization problem

$$\sum_{mm'} \phi_{jm}\, H_{mm'}\, \phi_{m'j'} = E_j\, \delta_{jj'} \tag{4}$$

for nuclear ground and excited states. If one chooses the main axes system of the EFG for reference, the matrix elements of the Hamiltonian for the excited nuclear state take

the form

$$(-1)^{m-m'}\,H_{mm'} = -\mu_N g'\,B' \frac{C(I'I'1;mm')}{C(I'I'1;I'I')} \mathcal{D}^{(1)}_{m-m'}\left(0,\beta',\gamma'\right) + \frac{1}{2} eQ'V_{zz} \frac{C(I'I'2;mm')}{2C(I'I'2;I'I')} \left\{ \delta_{mm'} + \frac{\eta}{6}\,\delta_{2,|m-m'|} \right\}, \qquad (5)$$

where the angles β' and γ' give the direction of the magnetic hyperfine field in the EFG system and $B' = |\mathbf{B} + \mathbf{B}_{\text{ext}}|$ is the effective magnetic field at the nucleus. $C(\ldots)$ and $\mathcal{D}$ are Clebsch–Gordan coefficients and rotation matrices, respectively, in the notation of Rose [20]. μ_{N} denotes the nuclear magneton.

Fluctuating hyperfine fields are treated by providing a set of hyperfine parameters $\{\delta E_0, eQ'V_{zz}/2, \eta, B, \xi_{\text{p}}, \xi_{\text{a}}, \theta, \varphi\}$ together with a matrix of transition rates describing the random jumps between the different hyperfine parameters. The main axes system of the EFG defined by the Euler angles $\alpha,\ \beta,\ \gamma$ is assumed static. The eigenvalue problem now takes the form

$$\sum_{mm'MM'\rho\sigma} L^{\mu\rho}_{jj'mm'} A^{\rho\sigma}_{mm'MM'} R^{\sigma\nu}_{MM'll'} = \Omega^{\mu}_{jj'} \delta_{\mu\nu}\delta_{jl}\delta_{j'l'}, \qquad (6)$$

where L, R are left and right eigenvectors and Ω are the new (complex) eigenvalues. The matrix A is constructed with the matrix elements given in eq. (5) and the transition matrix ($\lambda^{\rho\sigma}$):

$$A^{\rho\sigma}_{mm'MM'} = \mathrm{i}\lambda^{\rho\sigma}\delta_{mM}\delta_{m'M'} + H^{'\rho}_{m'M'}\delta_{mM}\delta_{\rho\sigma} - H^{\rho}_{mM}\delta_{m'M'}\delta_{\rho\sigma}. \qquad (7)$$

In this expression, $H^{\rho}_{mM} = \langle Im|\widehat{H}^{\rho}|IM\rangle$ and $H^{'\rho}_{m'M'} = \langle I'm'|\widehat{H}^{\rho}|I'M'\rangle$ are matrix elements of the Hamiltonian $\widehat{H}^{\rho}$ using spin eigenvectors for nuclear excited and ground states. The index ρ labels a particular set of hyperfine parameters. The transition matrix satisfies $\sum_{\sigma}\lambda^{\rho\sigma} = 0$.

The solutions of the eigenvalue problem defined either by eq. (4) or by eq. (6) will serve to calculate the coherent elastic scattering amplitude from a thin platelet. The formulas were explicitly given by Sturhahn and Gerdau [14] for the static case. The calculation of energy, angle and polarization-dependent transmission or reflectivity functions can be completed with information about scattering geometry, calculation ranges, and nonresonant atoms in the material. The needed parameters are listed in table 3. The program uses linear polarization vectors as a basis for the transmission or reflectivity matrices. When Bragg/Laue cases are calculated, σ-polarization for incident and diffracted radiation is defined perpendicular to the scattering plane as illustrated in figures 3 and 4. For cases of forward scattering, figure 2 shows that σ-polarization is defined perpendicular to the plane common to the incident wave vector and the external magnetic field. The π-polarization vectors are obtained from vector products of the σ-polarization vector with the corresponding wave vector.

At this point the energy, angle and polarization-dependent transmission or reflectivity functions for a particular material in a particular scattering geometry are

Table 4
Parameters characterizing polarization properties of incident radiation and the polarization sensivity of the detection system.

Symbol	Parameter
P	Degree of polarization of the incident radiation.
θ_{M}	Mixing angle of the incident radiation.
θ_{C}	Canting angle of the incident radiation.
P'	Filter efficiency of the detection system.
θ'_{M}	Mixing angle of the filtered detected radiation.
θ'_{C}	Canting angle of the filtered detected radiation.

completely defined. The program offers the flexibility to combine scatterers characterized in this way, i.e., the transmission or reflectivity matrices are multiplied according to the spatial arrangement of the corresponding samples. A time spectrum is now obtained by a Fourier transformation of the energy-dependent transmission or reflectivity functions. Such a time spectrum describes the response of the ensemble of nuclear resonant scatterers to a very short pulse of radiation. However, if the user wishes to calculate energy spectra, this step may be omitted and one obtains the response to monochromatic radiation. Therefore CONUSS can handle the calculation of conventional energy spectra as well as time spectra obtained with synchrotron radiation. Amplitude as well as phase of the scattered field are calculated and thus the full information is retained. The most relevant derived quantity is the intensity, which can be compared to results from usual experiments. At this point the polarization properties of incident synchrotron radiation and the polarization sensivity of the detection system must be defined. The CONUSS software uses the parameters listed in table 4. Assume the transmission function T was calculated for a particular energy or time in the basis of linear polarization vectors as described above. The intensity is then

$$I = \mathrm{Trace}\{\mathsf{D}\mathsf{T}^{\dagger}\mathsf{F}\,\mathsf{T}\}, \tag{8}$$

where D is the density matrix describing the polarization of the incident radiation, and F encompasses the polarization sensivity of the detector. These matrices can be expressed in a linear polarization basis as follows:

$$\begin{aligned}
\mathsf{D} &= \frac{1}{2}\begin{pmatrix} 1 + P\cos\theta_M\cos\theta_C & P(\sin\theta_C\cos\theta_M - \mathrm{i}\sin\theta_M) \\ P(\sin\theta_C\cos\theta_M + \mathrm{i}\sin\theta_M) & 1 - P\cos\theta_M\cos\theta_C \end{pmatrix}, \\
\mathsf{F} &= \frac{1}{2}\begin{pmatrix} 2 - P'(1 - \cos\theta'_M\cos\theta'_C) & P'(\sin\theta'_C\cos\theta'_M - \mathrm{i}\sin\theta'_M) \\ P'(\sin\theta'_C\cos\theta'_M + \mathrm{i}\sin\theta'_M) & 2 - P'(1 + \cos\theta'_M\cos\theta'_C) \end{pmatrix},
\end{aligned} \tag{9}$$

where the parameters are defined in table 4. This system offers great flexibility in probing the polarization dependence of NRS. Left- or right-circularly polarized radiation, e.g., is defined by $\theta_{\mathrm{M}} = \pm\pi/2$, and $\theta_{\mathrm{M}} = 0$ gives linear polarization. Intermediate values correspond to elliptically polarized states. The degree of polarization can be continuously adjusted between completely polarized, $P = 1$, to unpolarized $P = 0$.

The canting angles lead to a rotation of the base vectors and accommodate situations with varying directions of hyperfine fields relative to the polarization of the radiation.

2.2. Comparison to data

In the previous section, the calculation of a time spectrum starting from a collection of parameters that describe sample properties as well as geometrical constraints and ending with an intensity function was explained. Optionally one may also obtain energy spectra under identical conditions. It is practical to allow certain averaging procedures before the intensity function is directly compared to the measured data. The program permits convolution of the intensity function with either Gaussian (optionally asymmetric) and Lorentzian shape functions. Therefore a time spectrum can incorporate the detector resolution function, and an energy spectrum may be combined with the spectral function of a single line Mössbauer source. If Bragg or Laue reflections are studied, one can apply the convolutions to the angle coordinate, thus simulating the divergence of the incident radiation. In the case of forward scattering, such an averaging may be performed over the thickness parameter, thus simulating samples of varying thicknesses in the cross-section of the incident radiation. The calculation of the time spectrum assumes that the incident radiation consists of a single short pulse. The experimental data are often obtained under different conditions, i.e., synchrotron radiation is a periodic sequence of uncorrelated pulses. The user of CONUSS can define the pulse sequence, which is then used to construct an improved simulation from the intensity function. This is particularly important if the separation of the synchrotron radiation pulses is comparable to or even less than the lifetime of the nuclear resonance. The theoretical simulation that has been prepared in this way is then compared to measured data. Scaling factor and background are adjusted automatically to minimize the mean square deviation. This procedure constitutes the minimum of parameter adjustments that can take place. In general, the CONUSS software allows the automatic adjustment of every numerical input parameter including those specified in tables 1–4 with the aim to minimize the mean square deviation of calculation from measurement. More complex situations are accommodated by grouping of fit parameters, i.e., several parameters are simultaneously varied while keeping their relationship intact. Examples are variation of one quadrupole interaction in a system with many different magnetic hyperfine fields, or the variation of weights of different sites that should be kept normalized. The users of the CONUSS program are therefore offered great flexibility in the evaluation of data from samples important to their objectives.

2.3. Example evaluations

In the past years, the CONUSS software has been used by several scientists to evaluate a variety of time spectra. Some examples concerning nuclear resonant Bragg reflections were given earlier by Sturhahn and Gerdau [14]. Recently NFS received more attention, and therefore examples of evaluation of such time spectra obtained

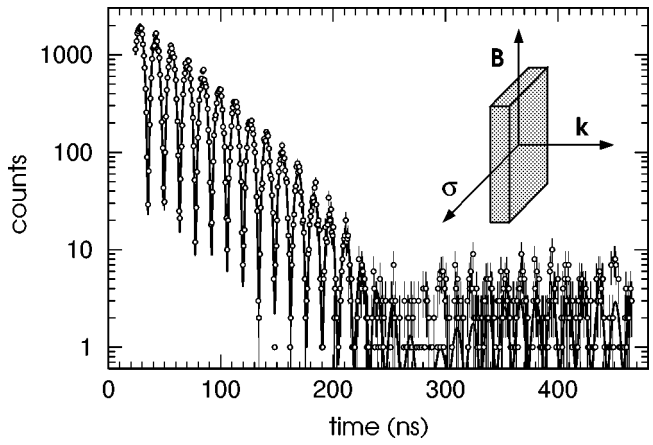

Figure 5. Time spectrum of an α-iron foil. The scattering geometry is shown as an inset. The incident synchrotron radiation is σ-polarized. The line was calculated using the CONUSS software. The data were taken from [21].

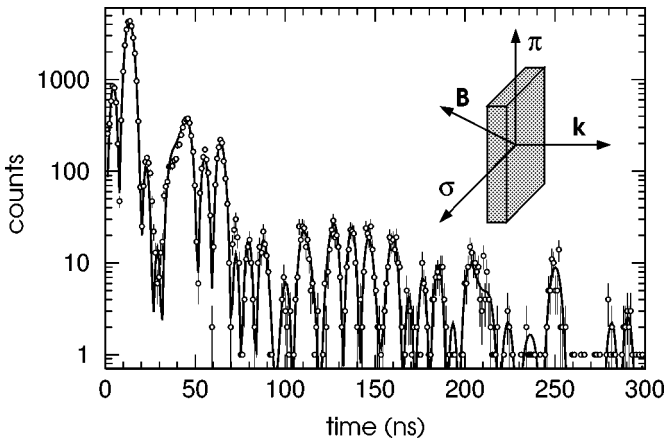

Figure 6. Time spectrum of an α-iron foil including polarization filtering. The scattering geometry is shown as an inset. The incident synchrotron radiation is σ-polarized and only the π-component of the transmitted radiation is detected. The line was calculated using the CONUSS software. The data were taken from [9].

with synchrotron radiation sources are presented. In addition, an evaluation of a conventional energy spectrum demonstrates the flexibility of the CONUSS software.

In figure 5, the time spectrum of an α-iron foil and the simulation obtained with CONUSS are shown. The data were taken from [21]. The measurement was performed under ambient conditions, and the scattering geometry is outlined in figure 5. With the procedure explained in the previous section, the magnetic field at the location of the nucleus and the effective thickness of the sample were adjusted. The results are $B = 32.7(2)$ T and $d = 14.9(15)$, where the value of B includes the applied external magnetic field of 0.13 T. Figure 6 shows the time spectrum of a different

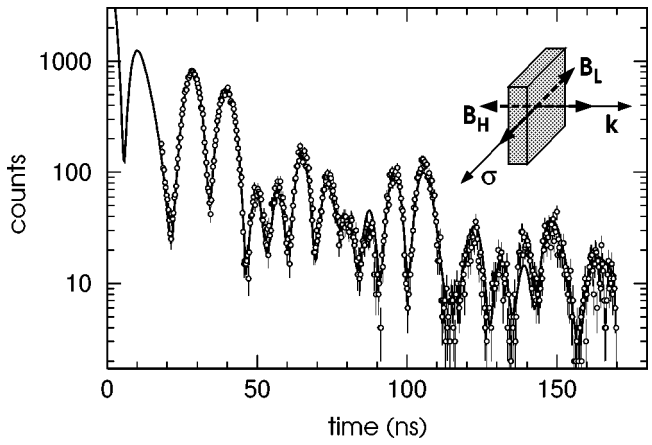

Figure 7. Time spectrum of a single crystal of Fe_3BO_6 at a temperature of 414.7 K. The line represents the calculation using the CONUSS software with hyperfine parameters supplied in table 5. The scattering geometry and the orientation of the magnetic hyperfine fields above and below the Morin transition are indicated. The data were provided by Jäschke et al. [22].

Table 5
Hyperfine parameters used to simulate a time spectrum of Fe_3BO_6 as shown in figure 7. The indices L and H indicate the magnetic structures as found below and above the Morin transition temperature. In the present data, one obtains for the ratio of the phases $H : L = 1 : 0.39(1)$. The effective thickness of the crystal was adjusted to 81(4).

Parameter	8d sites	4c sites
δE_0 (mm/s)	0	0.025
$eQ'V_{zz}/2$ (mm/s)	0.49	-0.91
η	0.93	0.83
α (deg.)	150 204 204 150	55 95
β_L (deg.)	28(5)	100(40)
β_H (deg.)	22(3)	20(3)
γ (deg.)	90	90
B (T)	32.2(2)	35.9(2)
θ_L (deg.)	90 90 270 270	90 270
θ_H (deg.)	0 0 180 180	0 180
φ (deg.)	0	0

α-iron foil measured with a polarizer–analyzer setup [9]. The time spectrum reflects the optical activity around the nuclear resonance and contains similar information about the hyperfine interactions as in the previous example. The calculation provides $B = 32.9(2)$ T and $d = 167(9)$.

However, the hyperfine parameters of α-iron are well known, and we proceed to more complicated cases. Using NFS, Jäschke et al. [22] investigated the Morin transition in single crystals of Fe_3BO_6. Time spectra were taken at several temperatures in the transition region around 414 K where the directions of the magnetic

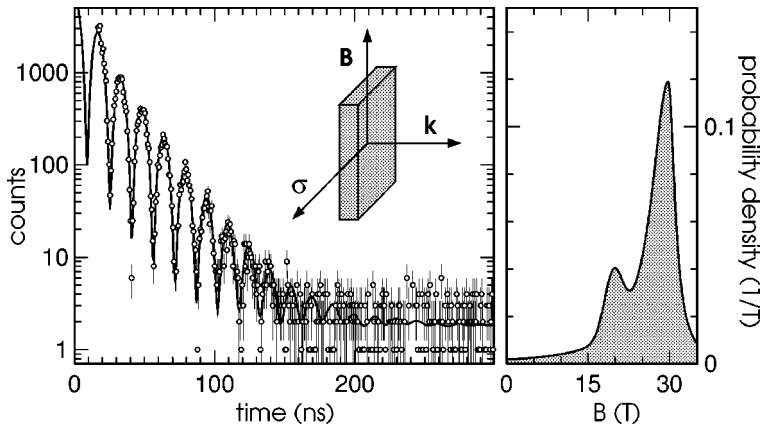

Figure 8. Time spectrum of an INVAR foil, $Fe_{65}Ni_{35}$. The line represents the calculation using the CONUSS software with the distribution function for the magnetic hyperfine fields shown in the right-hand graph. The scattering geometry is shown as an inset. The incident synchrotron radiation is σ-polarized. The data were taken from [21].

hyperfine fields change. The unit cell of Fe_3BO_6 contains four formula units and provides six sites with different hyperfine interactions for the iron nuclei. In the vicinity of the Morin transition, the time spectrum has to be simulated using 12 nuclear sites, i.e., six sites each for high and low temperature phases. The time spectrum in figure 7 is a sample from a series of more than 100 spectra. The hyperfine parameters shown in table 5 were used to reproduce the data with excellent quality. Errors are given for values that were adjusted by CONUSS using only this spectrum. The other values were obtained by Jäschke et al. from evaluation of all available time spectra. In the previous examples, the hyperfine fields were constant throughout the probed sample volume. Materials may show distributions of hyperfine fields, however. The CONUSS program accommodates such distributions if the sample is homogeneous within the coherent volume of the incident radiation. For many samples, this condition is satisfied. Figure 8 shows a time spectrum of an INVAR foil, $Fe_{65}Ni_{35}$, and the probability density of the magnetic hyperfine field that was used to produce the solid line. The data were provided by Shvyd'ko et al. [21]. In their paper, Shvyd'ko et al. used the MOTIF software [12] to evaluate the same data using an asymmetric magnetic hyperfine field distribution composed of three Gaussians. The field distribution in figure 8 was constructed from an asymmetric Lorentzian and a symmetric Gaussian. The quality of the data is not sufficient to determine the shape of the distribution function more accurately.

The last example of data evaluation with the CONUSS software is shown in figure 9. A foil of Fe_3Al alloy was investigated by NFS in combination with the polarizer–analyzer technique as well as with a conventional conversion electron Mössbauer spectroscopy (CEMS) setup. In both cases, the distribution of the magnetic hyperfine fields was determined. We find sharp peaks around 21.4 T and 30 T that correspond to Wyckoff 8c and 4b sites in the DO_3 structure of crystalline Fe_3Al. The

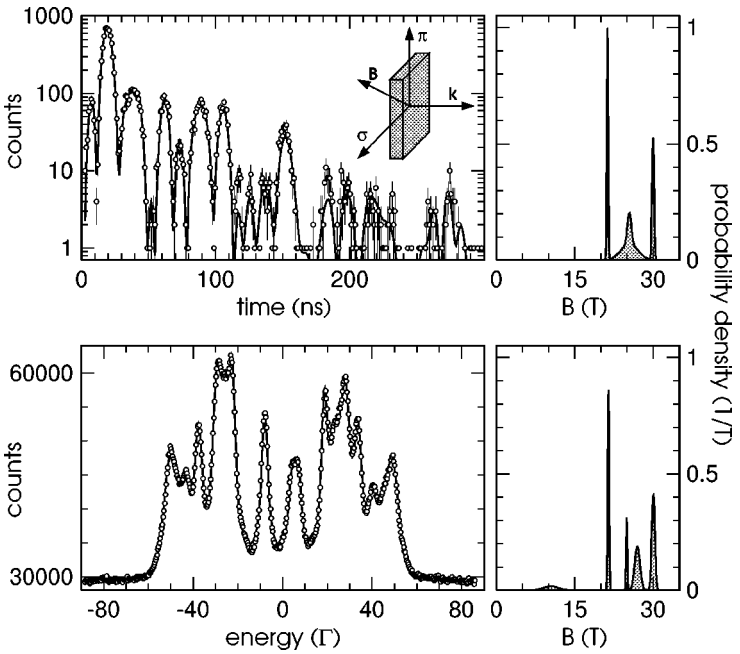

Figure 9. Time spectrum and CEMS spectrum of a Fe_3Al alloy. The time spectrum was obtained with a polarization filtering technique similar to the data in figure 6. The scattering geometry is shown as an inset. For both types of spectra, the line represents the calculation using the CONUSS software. The corresponding distribution functions of the magnetic hyperfine fields are shown on the right.

remaining features in the field distribution arise from residual disorder in the sample, probably due to the manufacturing process.[1] The discrepancies in hyperfine field distributions obtained from the different types of spectra reflect differences in surface (probed in CEMS) and volume properties of the sample.

The last example comprises a calculation of time spectra for a simple case of two-state magnetic relaxation using the Blume–Tjon mechanism. The results are shown in figure 10. The calculations were performed for a $1/2 \rightarrow 3/2$ nuclear transition. The two magnetic states are characterized by hyperfine fields of opposite sign. The magnitude of the hyperfine fields is equivalent to a separation of the outer lines of $100\,\Gamma$. The transition matrix used in eq. (7) assumed the form

$$\lambda \begin{pmatrix} -1 & 1 \\ 1 & -1 \end{pmatrix}, \tag{10}$$

where the relaxation rate λ appears as parameter in figure 10. The calculations leading to figure 10 assumed a polarizer–analyzer setup as described by Alp et al. [11] with a scattering geometry identical to the inset in figure 6. In the slow-relaxation limit, the image in figure 10 shows a pronounced oscillation pattern that is characteristic

[1] The Fe_3Al sample was provided by Prof. B. Fultz, California Institute of Technology. The manufacturing process is, e.g., described in [23].

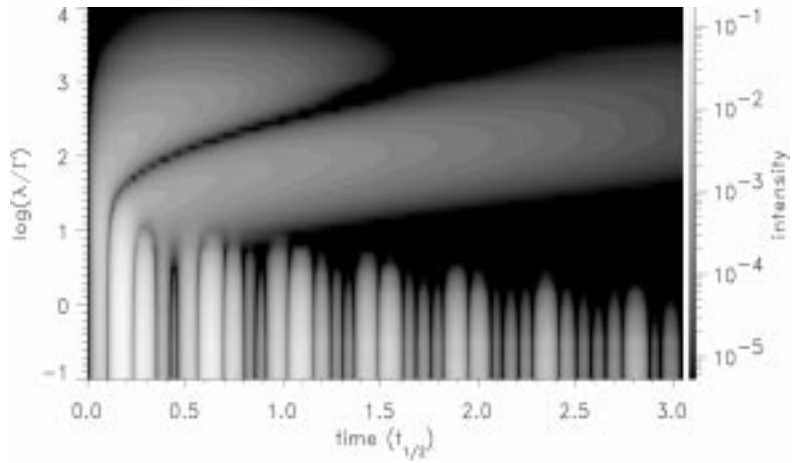

Figure 10. Calculated time spectra versus relaxation rate λ for a two-state magnetic relaxation model after Blume and Tjon. The transition matrix is given by eq. (10). Brighter areas indicate larger intensity values. The bar scale to the right shows the relationship between brightness and calculated intensity. The image shows the intensity that arises from σ-to-π scattering, i.e., one assumes the same polarization filtering technique that was applied to obtain the data of figure 6. Also the scattering geometry was adopted.

for the magnetic splitting. With increasing values of the relaxation rate, the decay of the oscillations accelerates but the pattern remains unchanged. Around $\lambda = 8\,\Gamma$, the time spectra change dramatically, indicating the collapse of the inner lines. In this region, the damping is strongest. For larger values of λ, the short-period oscillations disappear. The remaining slow modulation is essentially determined by the relaxation rate and the effective thickness of the sample, $d = 10$ in the present case. Finally, the fast-relaxation limit leaves only the dynamical oscillations arising from thickness effects. In addition, the optical activity of the sample, and thus the integrated intensity for a crossed-polarizer setup, vanishes. However, the use of a polarizer–analyzer setup seems appropriate for the experimental study of systems with relaxation behavior, because the early times in the decay pattern are more easily accessible, e.g., compare the spectra in figures 5 and 6.

3. The PHOENIX software

The spectra that are obtained in applications of incoherent NRS are quite different from the time spectra discussed in the previous section. If the nucleus is excited by pulsed synchrotron radiation, the discrimination of incoherent NRS events from electronic contributions proceeds very efficiently by counting delayed photons originating in either atomic or nuclear fluorescence. Tuning the energy of the incident synchrotron radiation with respect to the nuclear resonance while monitoring the total yield of the delayed fluorescence photons provides a superposition of all possible phonon excitations. The experimental details were elucidated by Chumakov and Sturhahn [24], and

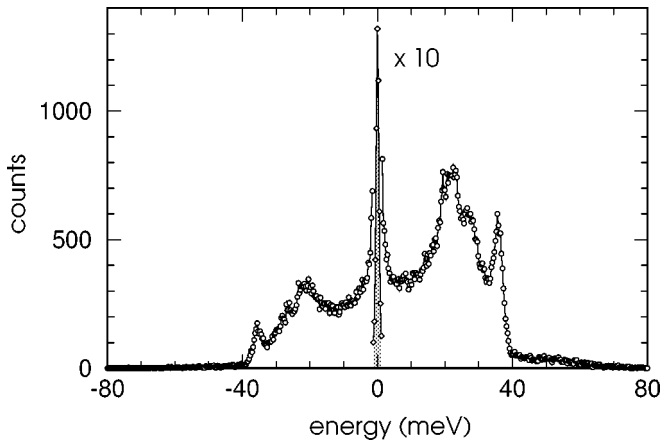

Figure 11. Incoherent NRS spectrum of an α-iron foil. The central region was multiplied by 0.1 to emphasize the inelastic components of the spectrum. The data were taken from [31].

theoretical aspects were studied by Sturhahn and Kohn [25]. The evaluation of spectra from incoherent NRS has been discussed by Sturhahn et al. [16], Kohn et al. [26], and Hu et al. [27]. A typical spectrum is shown in figure 11. The central, elastic peak indicates the energy of the nuclear transition. The left-hand side shows an energy transfer from lattice to nucleus that is equivalent to net-annihilation of vibrational quanta. Similarly, the right-hand side gives the net-creation term. The evaluation procedure consists of two steps:

- Determination of the elastic contribution to the spectrum by matching the resolution function to the central peak and calculation of several moments of the spectrum followed by normalization.
- Removal of the elastic contribution from the data, decomposition into n-phonon terms, and derivation of the partial phonon density of states (DOS).

3.1. Normalization and moments

The functional dependence of the measured curve can be described as

$$I(E) = \int R\big(E - E'\big)\big\{aS\big(E'\big) - b\delta\big(E'\big)\big\}\,\mathrm{d}E', \tag{11}$$

where E is the energy of the incident synchrotron radiation relative to the nuclear transition energy, $S(E)\,\mathrm{d}E$ is the probability for a vibrational excitation within the interval $[E, E + \mathrm{d}E]$, and R is the normalized resolution function of the monochromator. The coefficients a and b depend on the experimental conditions. In particular, a provides the data normalization, and its precise determination is crucial to the data evaluation procedure. The coefficient b quantifies saturation effects [16] that occur in the vicinity of the nuclear resonance. The correct zero-energy is found by a fit of the monochromator resolution function to the central peak. The user has the choice

Table 6
List of parameters needed by PHOENIX.

Symbol	Parameter
E_0	Nuclear transition energy.
E_R	Recoil energy of the free atom.
T	Temperature of the sample.
B_0	Background in measured data, e.g., detector noise.
E_F	Energy range of elastic peak, which will be adjusted to the resolution function in the interval $[-E_F, E_F]$.
c_2	Relative inelastic contribution under the elastic peak.
c_4	Left/right asymmetry of the resolution function.
c_5	Determines the shape of internally generated resolution functions.
δE	FWHM of a Gaussian used to smooth output data.

of specifying the resolution function of the monochromator either by file, e.g., from a separate measurement, or by a set of parameters that cause generation of a shape function internally. Table 6 gives the set of needed input parameters. The PHOENIX software adjusts the following function to the central area of the spectrum

$$P(E) = c_1\left\{ R(E - c_0) + c_2 \frac{\beta(E - c_0)}{1 - \mathrm{e}^{-\beta(E-c_0)}} \right\}, \tag{12}$$

where the parameters c_0, c_1, c_2 are adjustable and β is the inverse temperature. The second term comprises a background function that is equivalent to the one-phonon contribution from a Debye solid. The function R describes the shape of the elastic peak. In case the shape is specified by file in the form of the function H, the program uses

$$R(E) = \begin{cases} H\left[E\dfrac{2c_3}{1+c_4}\right], & E \geqslant 0, \\ H\left[E\dfrac{2c_3c_4}{1+c_4}\right], & E < 0, \end{cases} \tag{13}$$

where c_3 keeps the width adjustable and $c_4 \neq 1$ permits the introduction of asymmetry. If the user selects to generate the shape function internally, the dependence $H(x) = \exp(-|x|^{c_5})$ is used. The parameters c_{0-5} are optimized by minimizing the least squares deviation between resolution function and data. Now the zero and first-order moments of eq. (11) can be calculated, and values for the parameters a and b follow from Lipkin's sum rule $\int ES(E)\,\mathrm{d}E = E_\mathrm{R}$ [28], where E_R is the recoil energy of the free nucleus. The calculation of higher-order moments of S from measured data is described in detail by Hu et al. [27] and also by Sturhahn and Chumakov [29]. The second moment provides the average kinetic energy of the atom, and the third moment gives the average force constant for the atom. The PHOENIX software normalizes the spectrum and calculates several moments of the spectrum using these prescriptions.

3.2. Decomposition and partial phonon DOS

Further analysis of the data requires removal of the elastic contribution, i.e., $c_1 R(E-c_0)$ is subtracted from the spectrum. The Lamb–Mössbauer factor immediately follows:

$$f = 1 + \frac{c_1}{a} - \frac{1}{a}\int I(E)\,\mathrm{d}E. \tag{14}$$

At this point all information is prepared to decompose the measured spectrum into n-phonon contributions in accordance with the model of a harmonic lattice. We can write [16,25]

$$I(E) = c_1 R(E) + af \sum_{n=1}^{\infty} \int G_n\big(E'\big) R\big(E - E'\big)\mathrm{d}E', \tag{15}$$

where the energy scale is relative to c_0 and the n-phonon functions G_n depend recursively on the one-phonon function

$$G_{n+1}(E) = \frac{1}{n+1}\int G_n\big(E'\big) G_1\big(E - E'\big)\mathrm{d}E'. \tag{16}$$

Equations (15) and (16) have a simple form in reciprocal presentation that arises naturally in the discussion of the self-intermediate scattering function [25]. Indicating the Fourier image of a function with a tilde we obtain

$$\widetilde{G}_1 = \ln\left\{1 + \frac{\tilde{I} - c_1\widetilde{R}}{af\widetilde{R}}\right\}. \tag{17}$$

This convenient way of obtaining the one-phonon function is referred to as the *Fourier-log method* [30]. The problems that may arise from the deconvolution, i.e., the division by $\widetilde{R}$ in the previous equation, are addressed in a twofold way. A cutoff function ϕ is introduced, and the n-phonon functions are convoluted with the resolution function. The PHOENIX software produces the following results: the one-phonon contribution

$$S_1(E) = f\mathcal{F}^{-1}\left[\widetilde{R}\ln\left\{1 + \phi\frac{\tilde{I} - c_1\widetilde{R}}{af\widetilde{R}}\right\}\right], \tag{18}$$

the two-phonon contribution

$$S_2(E) = \frac{f}{2}\mathcal{F}^{-1}\left[\widetilde{R}\ln^2\left\{1 + \phi\frac{\tilde{I} - c_1\widetilde{R}}{af\widetilde{R}}\right\}\right], \tag{19}$$

and the higher-order contributions

$$S_{n>2}(E) = \frac{1}{a}\big\{I(E) - c_1 R(E)\big\} - S_1(E) - S_2(E). \tag{20}$$

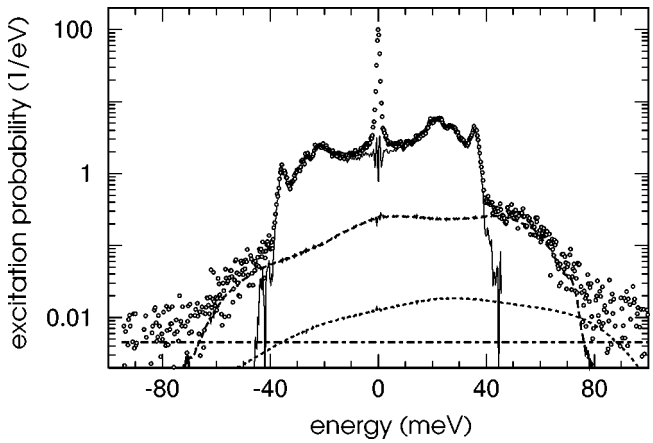

Figure 12. Decompostion of the incoherent NRS spectrum of an α-iron foil. The symbols represent the normalized data. Using the procedure described in the text, the PHOENIX software produces a one-phonon contribution (solid line), a two-phonon contribution (dashed line), and higher-order contributions (dotted line). The background is also indicated (dash-dotted line). The data were taken from [31].

In the previous expressions, $\mathcal{F}^{-1}$ stands for the inverse Fourier transform. The cutoff function is chosen as

$$\phi = \min\left\{1, \left|\frac{\tilde{I}\widetilde{R}(0)}{\widetilde{R}\tilde{I}(0)}\right|\right\}. \tag{21}$$

Figure 12 gives the result of the decomposition procedure when applied to the data shown in figure 11. The relationship between the one-phonon contribution as given by eq. (18) and the partial phonon DOS is material independent. The PHOENIX program uses the formula

$$g(E) = \frac{E}{E_R}\tanh\frac{\beta E}{2}\big(S_1(E) + S_1(-E)\big), \quad E \geqslant 0. \tag{22}$$

Figure 13 shows the partial phonon DOS derived from the data in figure 11. In this particular case of iron metal, the derived quantity is identical to the total phonon DOS. It should be noted that the Lamb–Mössbauer factor, as well as the decomposition of the spectrum into individual phonon contributions, critically depends on the removal procedure of the elastic peak. In particular, the shape of the inelastic background under the elastic peak is speculative. As mentioned earlier, the functional dependence chosen in eq. (12) is equivalent to the one-phonon contribution from a Debye solid. One can distinguish two situations that would lead to inaccurate results. Either the higher order phonon contributions are considerable around the central peak or the material is not Debye-like for small energies, i.e., the phonon DOS is not proportional to E^2. In the first case, one obtains an estimate by combination of the relationships

$$1 - f = S_1 + \sum_{n>1} S_n, \qquad \int S_n(E)\,\mathrm{d}E = f\frac{(-\ln f)^n}{n!}. \tag{23}$$

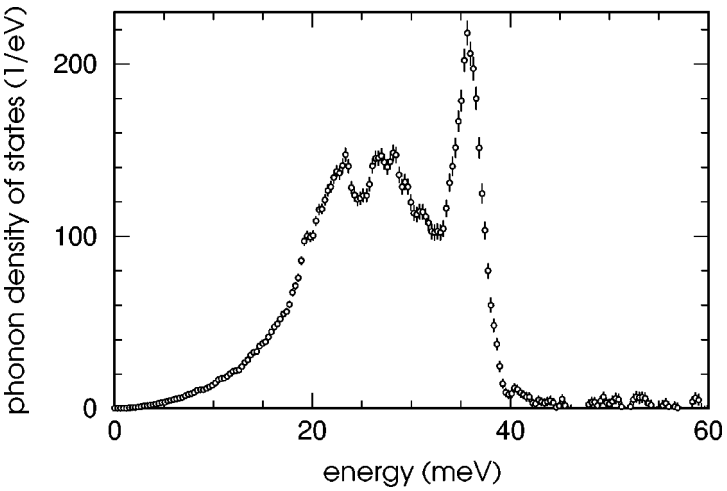

Figure 13. Phonon density of states of an α-iron foil. The procedure described in the text was applied to the data shown in figure 11. The error bars were obtained by propagating the statistical errors of the measured events.

The estimated relative contribution of higher order terms with $n > 1$ follows as $\gamma = 1 + f \ln f/(1-f)$. For $f = 0.8, 0.6, 0.4$, one obtains $\gamma = 0.11, 0.23, 0.39$, respectively. In principle, eventual deficiencies that may occur for small values of the Lamb–Mössbauer factor can be corrected by obtaining an improved shape for the background in a two-step procedure. After calculating a phonon DOS as described earlier in this section, one uses this function to calculate the higher order phonon terms and thus obtains the desired improvement.[2] The situation where the material is not Debye-like for small energies cannot be cured in a similar fashion by numerical tricks. However, consistency checks that are implemented in the PHOENIX software can give the needed help to decide upon the reliability of the decomposition procedure. It was mentioned earlier in the text that moments of the measured data of the type $\int E^n I(E)\,\mathrm{d}E$ for $n > 0$ can be calculated without removal of the elastic peak. One obtains the average kinetic energy from the second moment and the average force constant from the third moment. Both physical quantities can be equally calculated from the phonon DOS, and the results are compared with each other and the statistical error margins. Large deviations indicate either systematic errors in the data or an insufficient removal procedure for the central peak. Additional information can be derived from the left/right asymmetry (detailed balance) of the data, which is material independent. The PHOENIX program also provides error margins that are obtained by propagating the statistical uncertainties of the measured data.

[2] This procedure is not presently implemented in the PHOENIX software.

4. Conclusion

In this paper, the basic features of two software packages pertinent to the evaluation of NRS data were described. The CONUSS program was shown to be most useful for interpreting data obtained by nuclear forward scattering or nuclear Bragg/Laue scattering. This software offers ample flexibility to produce theoretical predictions of time spectra, CEM spectra, and Mössbauer transmission spectra for given sets of nuclear hyperfine parameters. The capability of adjusting such parameters automatically to measured data makes CONUSS a valuable tool for an extended range of coherent elastic NRS techniques. The PHOENIX software is designed to guide evaluation of data from the recently advanced incoherent NRS technique. The program derives several parameters characterizing the binding of atoms containing a resonant nucleus to neighboring atoms. The partial phonon density of states, an important quantity in understanding lattice dynamics, is extracted. In summary, a continuous development of instruments and methods furthered the potential of NRS applications with synchrotron radiation in the past decade. The software packages presented in this paper are designed to meet the natural need for evaluation and understanding of the measured data.

Acknowledgements

I am pleased to thank E. Gerdau and J. Jäschke for freely providing the Fe_3BO_6 data prior to publication. My gratitude also goes to Yu. Shvyd'ko for placing data at my disposal and to B. Fultz for providing the Fe_3Al sample. R. Rüffer and E. Gerdau are acknowledged for support in the early stages of the development of the CONUSS software. Finally, I express my thanks to E.E. Alp and T.S. Toellner for fruitful discussions. This work was supported by the U.S. Department of Energy, Basic Energy Sciences, Office of Science, under Contract No. W-31-109-Eng-38.

Appendix

This appendix presents calculations of integrated delayed counting rates that can be achieved in NFS experiments. The CONUSS software was used. Figure 14 provides the results for typical scenarios with static hyperfine interactions, i.e., magnetically split samples (six-line pattern, separation of outer lines $110\,\Gamma$), quadrupole split samples (two-line pattern, splitting $10\,\Gamma$), and unsplit samples, where Γ is the natural linewidth of the excited nuclear state. In each case, the effective thickness of the sample was varied over 5 orders of magnitude starting at 0.1. In addition, results for magnetic hyperfine field distributions and for two-state magnetic relaxation (Blume–Tjon mechanism) are shown in figures 15 and 16, respectively. In the relaxation case, the two magnetic states are characterized by hyperfine fields of opposite sign and a magnitude that is equivalent to a separation of the outer lines of $100\,\Gamma$. In all calculations, the field directions are randomly distributed. In the relaxation case, the

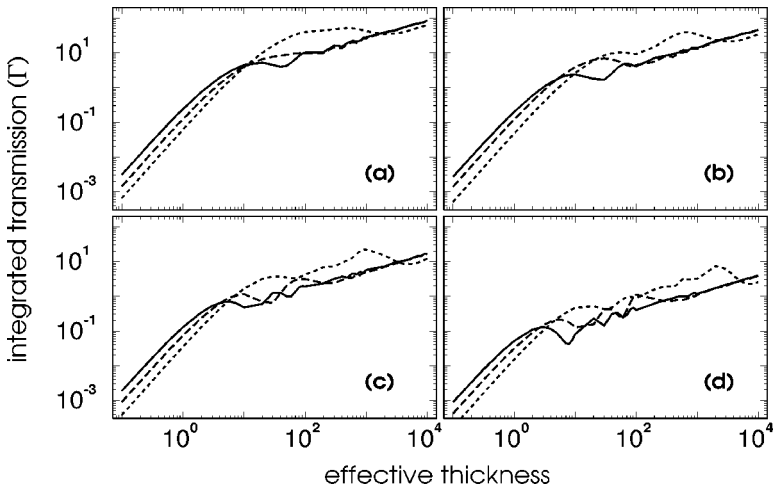

Figure 14. Integrated transmission for discrete static hyperfine interactions. The nuclear forward scattering signal was integrated over time regions starting at 30% (a), 50% (b), 100% (c), and 200% (d) of the half lifetime of the nuclear excited state. The calculations were performed for an unsplit resonance (solid lines), for two-line quadrupole splitting of $10\,\Gamma$ (dashed lines), and for six-line magnetic splitting of $110\,\Gamma$ (dotted lines). The field directions were randomly distributed. The fluctuations of the integrated transmission at larger effective thicknesses originate in dynamical oscillations in the time spectra that are truncated at the beginning of the integration region.

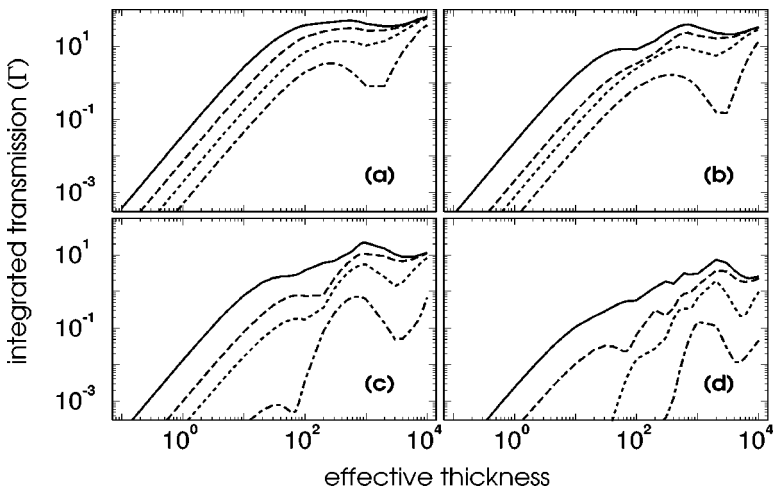

Figure 15. Integrated transmission for a Gaussian distribution of static magnetic hyperfine fields. The nuclear forward scattering signal was integrated over time regions starting at 30% (a), 50% (b), 100% (c), and 200% (d) of the half lifetime of the nuclear excited state. The six-line pattern with a $110\,\Gamma$ separation of the outer lines was broadened by Gaussian distributions with 1% (solid lines), 5% (dashed lines), 10% (dotted lines), and 20% (dash-dotted lines) FWHM. The field directions were randomly distributed. The fluctuations of the integrated transmission at larger effective thicknesses originate in dynamical oscillations in the time spectra that are truncated at the beginning of the integration region.

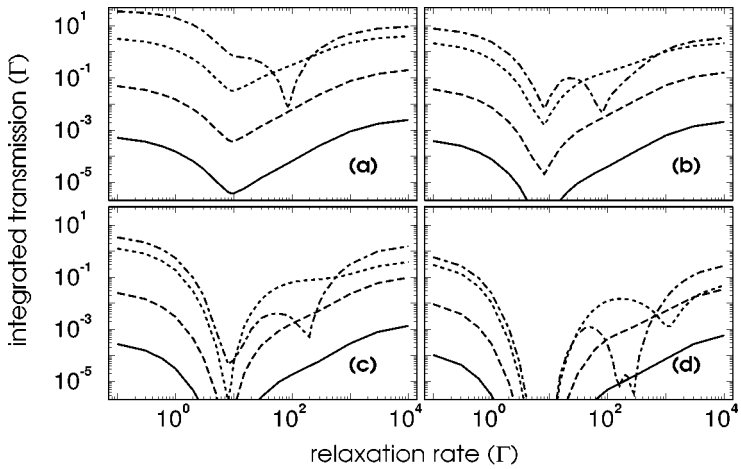

Figure 16. Integrated transmission for Blume–Tjon relaxation versus the relaxation rate in units of natural linewidths (Γ) of the excited nuclear state. Two magnetic hyperfine fields of 100 Γ separation of the outer lines but with opposite sign coexist. The field directions were randomly distributed. The nuclear forward scattering signal was integrated over time regions starting at 30% (a), 50% (b), 100% (c), and 200% (d) of the half lifetime of the nuclear excited state. The effective thicknesses are 0.1 (solid lines), 1 (dashed lines), 10 (dotted lines), and 100 (dash-dotted lines). The deep minima in the integrated transmission indicate a collapse of spectral lines that is accompanied by strong damping and very fast decay (see also figure 10 and the related discussion in the text).

transition matrix is given by eq. (10), where the relaxation rate λ is used as abcissa in figure 16. The selected time regions for the integration start at 0.3, 0.5, 1, 2 times the nuclear half lifetime $t_{1/2}$ and extend up to $30t_{1/2}$. The calculations were performed for a $1/2 \rightarrow 3/2$ nuclear transition. The integrated delayed intensities are given in units of Γ and do not consider electronic absorption. Hereafter, an example is given to demonstrate the use of the presented graphs for evaluating delayed counting rates for a particular situation. Please note that the given counting rates must still be reduced by the detector efficiency to obtain realistic results.

Consider, for example, a magnetically split sample containing ^{57}Fe to be studied by NFS. The detector system permits us to start the collection of delayed events after 30 ns $= 0.3t_{1/2}$. The effective thickness of the sample is 10. The transmitted intensity is reduced by a factor of 100 due to electronic absorption. The spectral intensity of the synchrotron radiation source is 4700 Hz/Γ. From figure 14(a) we read off an integrated delayed intensity of 3.8 Γ. Using the source intensity and the correction for electronic absorption, we expect 190 cps for the integrated delayed counting rate. For a complete assessment, the characteristics of the detector system and the energy width of the incident synchrotron radiation must be known. With 40% detector efficiency, the expected counting rate is reduced to 76 cps. However, one has to assure that the total measured photon flux (including the “prompt” counting rate) is below the saturation limit of the detector system. With an incident energy bandwidth of 1 meV, we calculate 4 MHz for the total measured photon flux. Avalanche photodiodes that are common

for this type of measurement easily withstand 10^7 Hz and will not add constraints in this example.

In summary, the following information is needed for a realistic assessment of counting rates in nuclear forward scattering experiments:

- $t_{1/2}$ and Γ,
- type of hyperfine interaction that is expected,
- effective thickness,
- reduction of transmission due to electronic absorption,
- starting time of observation window after prompt pulse,
- efficiency of detector,
- maximum measurable photon flux,
- spectral intensity of synchrotron radiation,
- energy bandwidth of synchrotron radiation.

References

[1] E. Gerdau and H. de Waard (eds.), *Nuclear Resonant Scattering of Synchrotron Radiation*, Hyp. Interact. 123–125 (1999/2000).
[2] E. Gerdau, R. Rüffer, H. Winkler, W. Tolksdorf, C.P. Klages and J.P. Hannon, Phys. Rev. Lett. 54 (1985) 835.
[3] E. Gerdau, R. Rüffer, R. Hollatz and J.P. Hannon, Phys. Rev. Lett. 54 (1986) 1141.
[4] G. Faigel, D.P. Siddons, J.B. Hastings, P.E. Haustein, J.R. Grover, J.P. Remeika and A.S. Cooper, Phys. Rev. Lett. 58 (1987) 2699.
[5] U. van Bürck, R.L. Mössbauer, E. Gerdau, R. Rüffer, R. Hollatz, G.V. Smirnov and J.P. Hannon, Phys. Rev. Lett. 59 (1987) 355.
[6] U. van Bürck, R.L. Mössbauer, E. Gerdau, W. Sturhahn, H.D. Rüter, R. Rüffer, A.I. Chumakov, M.V. Zelepukhin and G.V. Smirnov, Europhys. Lett. 13 (1990) 371.
[7] J.B. Hastings, D.P. Siddons, U. van Bürck, R. Hollatz and U. Bergmann, Phys. Rev. Lett. 66 (1991) 770.
[8] S. Kishimoto, Rev. Sci. Instrum. 63 (1992) 824.
[9] T.S. Toellner, E.E. Alp, W. Sturhahn, T.M. Mooney, X.W. Zhang, M. Ando, Y. Yoda and S. Kikuta, Appl. Phys. Lett. 67 (1995) 1993.
[10] D.P. Siddons, J.B. Hastings, U. Bergmann, F. Sette and M. Krisch, Nucl. Instrum. Methods B 103 (1995) 371.
[11] E.E. Alp, W. Sturhahn and T.S. Toellner, this issue, section VII-1.
[12] Yu.V. Shvyd'ko, this issue, section VIII-2.
[13] W. Sturhahn, Ph.D. thesis, Universität Hamburg (1991).
[14] W. Sturhahn and E. Gerdau, Phys. Rev. B 49 (1994) 9285.
[15] M. Seto, Y. Yoda, S. Kikuta, X.W. Zhang and M. Ando, Phys. Rev. Lett. 74 (1995) 3828.
[16] W. Sturhahn, T.S. Toellner, E.E. Alp, X.W. Zhang, M. Ando, Y. Yoda, S. Kikuta, M. Seto, C.W. Kimball and B. Dabrowski, Phys. Rev. Lett. 74 (1995) 3832.
[17] A.I. Chumakov, R. Rüffer, H. Grünsteudel, H.F. Grünsteudel, G. Grübel, J. Metge and H.A. Goodwin, Europhys. Lett. 30 (1995) 427.
[18] J.P. Hannon and G.T. Trammell, Phys. Rev. 169 (1968) 315; and 186 (1969) 306.
[19] M. Blume and J.A. Tjon, Phys. Rev. 165 (1968) 446.

[20] M.E. Rose, *Elementary Theory of Angular Momentum* (Wiley, New York, 1957).
[21] Yu.V. Shvyd'ko, U. van Bürck, W. Potzel, P. Schindelmann, E. Gerdau, O. Leupold, J. Metge, H.D. Rüter and G.V. Smirnov, Phys. Rev. 57 (1998) 3552.
[22] J. Jäschke et al., Universität Hamburg, unpublished (1999).
[23] T.A. Stevens and B. Fultz, Phys. Rev. Lett. 78 (1997) 366.
[24] A.I. Chumakov and W. Sturhahn, this issue, section V-1.1.
[25] W. Sturhahn and V.G. Kohn, this issue, section III-2.2.
[26] V.G. Kohn, A.I. Chumakov and R. Rüffer, Phys. Rev. B 58 (1998) 8437.
[27] M.Y. Hu, W. Sturhahn, T.S. Toellner, P.M. Hession, J.P. Sutter and E.E. Alp, Nucl. Instrum. Methods A 428 (1999) 551.
[28] H.J. Lipkin, Ann. Phys. 9 (1960) 332; Phys. Rev. B 52 (1995) 10073.
[29] W. Sturhahn and A.I. Chumakov, this issue, section V-1.2.
[30] D.W. Johnson and J.C.H. Spence, J. Phys. D 7 (1974) 771.
[31] T.S. Toellner, M. Hu, W. Sturhahn, K.W. Quast and E.E. Alp, Appl. Phys. Lett. 71 (1997) 2112.